

Preclinical Single Photon Emission Computed Tomography of Alpha Particle-Emitting Radium-223

Diane S. Abou,^{1-4,*} Andrew Rittenbach,^{5,*} Ryan E. Tomlinson,⁶ Paige A. Finley,⁷ Benjamin Tsui,⁷ Brian W. Simons,⁸ Abhinav K. Jha,^{1,9} David Ulmert,^{10,11} Ryan C. Riddle,¹² and Daniel L.J. Thorek^{1,2,4,9}

Abstract

Objective: Dose optimization and pharmacokinetic evaluation of α -particle emitting radium-223 dichloride ($^{223}\text{RaCl}_2$) by planar γ -camera or single photon emission computed tomography (SPECT) imaging are hampered by the low photon abundance and injected activities. In this study, we demonstrate SPECT of ^{223}Ra using phantoms and small animal *in vivo* models.

Methods: Line phantoms and mice bearing ^{223}Ra were imaged using a dedicated small animal SPECT by detecting the low-energy photon emissions from ^{223}Ra . Localization of the therapeutic agent was verified by whole-body and whole-limb autoradiography and its radiobiological effect confirmed by immunofluorescence.

Results: A state-of-the-art commercial small animal SPECT system equipped with a highly sensitive collimator enables collection of sufficient counts for three-dimensional reconstruction at reasonable administered activities and acquisition times. Line sources of ^{223}Ra in both air and in a water scattering phantom gave a line spread function with a full-width-at-half-maximum of 1.45 mm. Early and late-phase imaging of the pharmacokinetics of the radiopharmaceutical were captured. Uptake at sites of active bone remodeling was correlated with DNA damage from the α particle emissions.

Conclusions: This work demonstrates the capability to noninvasively define the distribution of $^{223}\text{RaCl}_2$, a recently approved α -particle-emitting radionuclide. This approach allows quantitative assessment of ^{223}Ra distribution and may assist radiation-dose optimization strategies to improve therapeutic response and ultimately to enable personalized treatment planning.

Keywords: α -particle radiotherapy, molecular imaging, pharmacokinetics, theranostics

Introduction

Prostate cancer afflicts nearly one in seven men globally.¹ When detected early and confined to the organ, it can be successfully treated with external beam radiotherapy or surgery. However, there is no effective long-term treatment for

non-organ confined and metastatic prostate cancer. Disseminated disease is often treated primarily with hormonal therapy, to which prostate cancer inevitably develops resistance. This fatal stage of the disease is characterized by metastatic seeding of the axial and then appendicular skeleton. Osseous metastases are often painful, reduce bone

¹Department of Radiology, Washington University School of Medicine, St. Louis, Missouri, USA.

²Program in Quantitative Molecular Therapeutics, Washington University School of Medicine, St. Louis, Missouri, USA.

³Radiology Cyclotron Facility, Mallinckrodt Institute of Radiology, Washington University in St. Louis, St. Louis, Missouri, USA.

⁴Oncologic Imaging Program, Siteman Cancer Center, Washington University School of Medicine, St. Louis, Missouri, USA.

⁵Information Sciences Institute, University of Southern California, Los Angeles, California, USA.

⁶Department of Orthopaedic Surgery, Thomas Jefferson University, Philadelphia, Pennsylvania, USA.

⁷Department of Radiology and Radiological Sciences, Johns Hopkins University School of Medicine, Baltimore, Maryland, USA.

⁸Center for Comparative Medicine, Baylor College of Medicine, Houston, Texas, USA.

⁹Department of Biomedical Engineering, Washington University, St. Louis, Missouri, USA.

¹⁰Department of Molecular and Medical Pharmacology, University of California Los Angeles, Los Angeles, California, USA.

¹¹Division of Urological Research, Department of Clinical Sciences, Lund University, Malmö, Sweden.

¹²Department of Orthopaedic Surgery, Johns Hopkins University School of Medicine, Baltimore, Maryland, USA.

*These two authors are co-authors.

Address correspondence to: Daniel L.J. Thorek; Department of Radiology; Washington University School of Medicine, 4939 Children's Place, Room 4401 CSRB, St. Louis, MO 63110, USA
E-mail: thorek.lab@wustl.edu

quality, reduce structural integrity leading to fracture, and invade the bone marrow and its hematological and stromal compartments. Bone metastases contribute to significant disability and eventually death.^{2,3}

Radium-223 dichloride ($^{223}\text{RaCl}_2$) is a recently approved α -particle-emitting radiopharmaceutical for application in men with castration-resistant metastatic prostate cancer. The radiotherapy agent demonstrated an improved median survival benefit of ~ 14 weeks versus placebo in a large-scale Phase III clinical trial.⁴ Subsequent subgroup analysis endorse these results, even for patients pretreated with chemotherapy. The α -particle endoradiotherapy approach also provided palliative relief, extended time to first symptomatic skeletal event, and reduced incidence of spinal cord compression.^{5,6}

Radium is a divalent cation that is thought to be incorporated within the bone matrix at sites of active remodeling as a calcium-mimetic agent. Most of the 28.2 MeV emitted by ^{223}Ra and its decay chain is in the form of four α particles. These charged helium nuclei exhibit high linear energy transfer, damaging nearby cells while sparing distant tissues from ionizing radiation.

The efficacy of the treatment combined with its favorable toxicity profile has encouraged the investigation of strategies toward improved and extended dosing (ClinicalTrials.gov identifier: NCT02023697 and NCT01934790). At present, $^{223}\text{RaCl}_2$ is administered on a per weight basis independent of patient disease characteristics or specific uptake distributions. To facilitate improved and personalized treatment regimes and to predict response, several imaging initiatives have been undertaken. Research has focused on imaging of either surrogate bone scan agents (such as $^{99\text{m}}\text{Tc}$ -methyl diphosphonate or [^{18}F]-NaF) or direct ^{223}Ra emissions to plan therapy.^{7,8}

Direct determination of uptake at sites of disease using ^{223}Ra itself has thus far been limited to scintigraphic imaging in men.⁹ These efforts are confined to planar scans, as count rates have been deemed insufficient for single photon emission computed tomography (SPECT) reconstruction. Efforts to quantitate images are in the early stages, but are restricted by low count rate, substantial scatter, and attenuation.^{10–12} Despite the difficulties, these studies have revealed important features of the *in vivo* fate of the radionuclide. Of note, a considerable proportion of the initial activity is rapidly incorporated into the gastrointestinal tract and excreted. Adverse events caused by dose adsorbed here include intractable nausea and gastrointestinal symptoms (diarrhea, constipation, and loss of appetite), which may lead to cessation of treatment.¹³

We have recently shown that the pharmacokinetics of ^{223}Ra in animal models recapitulates those found in men using *ex vivo* measures including γ -counting, α -camera imaging and whole-body autoradiography.¹⁴ This establishes murine models as an attractive platform to better understand the effects of and to optimize treatment with ^{223}Ra . Exciting developments in the SPECT field with respect to both instrumentation and reconstruction have motivated development of next-generation preclinical systems. High-resolution and sensitivity of imaging and therapeutic radionuclides in preclinical models have yielded insight into experimental agent development down to resolution as low as 0.25 mm.^{15–17} Here we report the application of tomographic imaging of radium-

^{223}Ra in mice for noninvasive delineation of radionuclide distribution at sub-microcurie injected activities with the potential to monitor dose distribution in real time.

Methods

Radium-223 and characterization

$^{223}\text{RaCl}_2$ was produced using a laboratory-built Actinium-227 microgenerator, as previously detailed.¹⁸ In brief, methanol/nitric acid was used to elute radium-223 from parental ^{227}Ac and ^{227}Th . Using strong anion exchange chromatography, the purified material (solvated in 0.03 M citrate) was verified using a high purity germanium γ -spectrometer (Detective-EX-100; Ortec). For the representative spectrum, a column fraction was placed on a platform at a distance of 2 cm from the detector and counted for 300 s. Spectra were initially analyzed in the Maestro software package (Ortec). A background spectrum (in the absence of a radioactive sample) was also acquired for 360 s with no detection of activity. Annotation of the spectra was provided from the Evaluated Nuclear Structure Data File hosted at the National Nuclear Data Center.¹⁹

Imaging system

The U-SPECT system (MILabs, Utrecht, the Netherlands) is a dedicated preclinical imaging platform. It comprises three large panel ($51 \times 38 \text{ cm}^2$) NaI detectors (9.5 mm thick crystals) with digital electronics providing full list mode acquisition, arranged in a triangular configuration. Subjects are placed in a multi-pinhole collimator by insertion on an automated (motion-controlled) and heated bed. The XUHS multi-pinhole tungsten collimator (54 pinholes of 2.0 mm diameter per pinhole, 48 mm tube diameter; MILabs) used in this study has a maximum resolution of 0.85 mm, and sensitivity of >13 kcps/MBq or 1.3% for $^{99\text{m}}\text{Tc}$.¹⁶ The animal was placed on a heated imaging bed with integrated inhalation anesthesia, which was translated through the center of the SPECT system in a spiral trajectory for imaging a selected region of the animal (defined for these studies as the whole body). Data are collected in list mode. Reconstruction at a 0.4 mm^3 consisted of a pixel-based ordered subset expectation maximization algorithm, using the U-SPECT reconstruction software,^{17,20} using 8 subsets and 10 iterations, without postreconstruction filters. Here, advanced resolution recovery based on a measured and interpolated position dependent point spread function compensates for distance-dependent sensitivity and blur is applied within user selected energy windows (below). Attenuation compensation was not applied. Scatter and background were compensated for with the triple-energy-window method²¹ with the main photopeak set for 75–100 keV with background windows of 70–75 keV and 100–105 keV.

Phantom studies

Line source phantoms each consisted of capillary tubes (1.0 mm outer diameter, 0.5 mm inner diameter; Sutter Instrument Company) filled with $^{223}\text{RaCl}_2$ in 0.03 M sodium citrate and stoppered with capillary tube sealant clay (Globe Scientific). Activity in each phantom was assessed using a CRC-127R dose calibrator (Capintec Inc.). Radium-223 was calibrated according to the guidelines provided by the

supplier in response to the U.S. Nuclear Regulatory Commission.²² Specifically, the dial setting of the calibrator was determined to match a decay corrected National Institutes of Standards and Technology calibrated clinical dose of $^{223}\text{RaCl}_2$ (Xofigo; Bayer Health Care Pharmaceuticals). This empirically determined dial setting was 277.

The scattering phantom was constructed by casting a 1% (w/v) agar gel (Invitrogen) in a 10 mL syringe. When set, this formed a cylinder of 99% water with a diameter of 1.6 cm in which the capillary tube was embedded. The scattering phantom with the capillary tube was then centered in the field of view of the small animal SPECT system. Imaging of the phantom was performed using a single frame for 30 min. Postacquisition reconstruction was performed with an energy window of 75–100 keV to capture the ^{223}Ra γ -emissions at 81, 83.8, 94.3, 94.9, and 97.5 keV.

X-ray computed tomography (CT) was performed on a Sedecal SuperArgus R4 small animal PET/CT (Sedecal Systems). Reconstructed SPECT/CT fusions were generated using a three-dimensional (3D) data visualization suite registration package (Amira version 5.3.3; FEI Inc.).

Animal studies

Radium-223 imaging. The Institutional Animal Care and Use Committee of the Johns Hopkins University approved all procedures involving mice. C57Bl/6 mice were purchased from Charles River, all mice were male with weight between 22 and 27 g (5–7 weeks old). Animals were induced and maintained at the plane of anesthesia using isoflurane, and $^{223}\text{RaCl}_2$ in citrate was administered by retro-orbital injection in $\sim 100 \mu\text{L}$. As described previously, animal images were acquired with the small animal U-SPECT system using a highly sensitive multipinhole collimator (the MILab XUHS collimator) on a heated bed with built-in anesthetic gas flow. The field of view for the acquisitions was set at $28 \times 28 \times 70 \text{ mm}$ for all subjects. Generally, we acquired four frames of 22 min each, which were averaged for reconstruction (using the energy windows described in “Results” section). The total scan time including bed motion and positioning of the animals was $\sim 90 \text{ min}$. CT on the same animals was acquired as above, using the Sedecal SuperArgus R4.

Bone scan. A representative mouse bone scan was acquired using a 44 mm inner diameter, 1.0 mm diameter multipinhole collimator. The anesthetized mouse was administered 37 MBq $^{99\text{m}}\text{Tc-MDP}$ (Cardinal Health) by retro-orbital injection. Imaging on the U-SPECT was performed 25 min after injection, using a single frame for 25 min.

Autoradiography. Whole-body and hind-limb specimens were flash frozen in optimal cutting temperature media (Sakura Fintec) and submerged in liquid nitrogen. Whole-body autoradiography was performed using the Bright 8250 Cryostat (Bright Instruments) and sections of limbs were obtained using a modified cryotome (Leica 1800). En bloc images of sections ($10 \mu\text{m}$ in thickness) were acquired, as previously described.¹⁴ Sections were exposed on phosphor screens and imaged using a desktop phosphor imaging scanner (Cyclone Phosphor Imager; Packard).

Histology. Reagents were purchased from ThermoFisher Scientific unless otherwise identified. Immunofluorescence labeling of fresh-frozen sections was performed with γH2AX rabbit antimouse antibody (Ab-139; Sigma-Aldrich). Fresh-frozen sections were bathed in room temperature 10% paraformaldehyde for 10 min, washed with phosphate-buffered saline (PBS), and then blocked with goat serum for 1 h. The primary antibody was diluted to 1:250 in PBS and incubated overnight at 4°C . Alexa488-conjugated goat anti-rabbit secondary was diluted 1:200 and applied to the PBS washed slides for 1 h at 4°C . Sections were counterstained with Hoechst 33342 for 5 min and washed in triplicate with PBS before mounting in an aqueous glycerol (30% v/v), and letting set overnight.

Results

Characterizing imaging properties of radium-223

The γ ray spectra of radium-223 and daughter radionuclides (including radon-219, lead-211, and bismuth-211) were measured using a high-resolution high-purity germanium (HPGe) detector, as given in Figure 1A. While $<2\%$ of the energy of the emitted energy of ^{223}Ra and daughters is in the form of photons, it can be seen that there are characteristic emissions present for *in vivo* imaging. The NaI(Tl) detectors used in the camera of the small animal U-SPECT system are of significantly poorer energy resolution than the cryo-cooled HPGe system. To determine if the U-SPECT could be used to detect and quantify low (biologically relevant) levels of ^{223}Ra , a glass capillary tube of 22 kBq ($0.59 \mu\text{Ci}$) of activity was evaluated. A representative, normalized spectra of the rod phantom from one of the three γ -camera heads from a 10-min acquisition is shown (Fig. 1B). As expected, individual emissions are no longer discernable, however the prominent ^{223}Ra γ -rays are apparent.

Phantom imaging of radium-223 sources

A line source with 23.5 kBq ^{223}Ra was imaged to determine if sufficient counts could be provided for SPECT reconstruction. A list-mode acquisition of 480 min was performed using the 75–100 keV energy window. Different fractions of the list-mode data with different totals of acquired counts were used in reconstruction to evaluate the effects of low counting statistics. We found that the small animal SPECT system provided adequate photon detection sensitivity to provide sufficient detected counts in a reasonable acquisition time (1 h) for image reconstruction (Fig. 1C).

To evaluate the quantitative accuracy of the SPECT system, samples were imaged following a system calibration with a NIST-standardized ^{223}Ra source. Solutions of $^{223}\text{RaCl}_2$ dissolved in 0.03 M citrate buffer in 0.2 mL Eppendorf microcentrifuge tubes were imaged in the scanner. Volumes of interest of the different activity levels were manually drawn in the reconstructed datasets and plotted relative to the known activity (Fig. 1D). Representative fusion of the SPECT and CT volumes of the tubes are given in Figure 1E.

Tissue phantom imaging of radium-223

The photon emissions from ^{223}Ra used in SPECT imaging are in the range of energies that can be scattered heavily

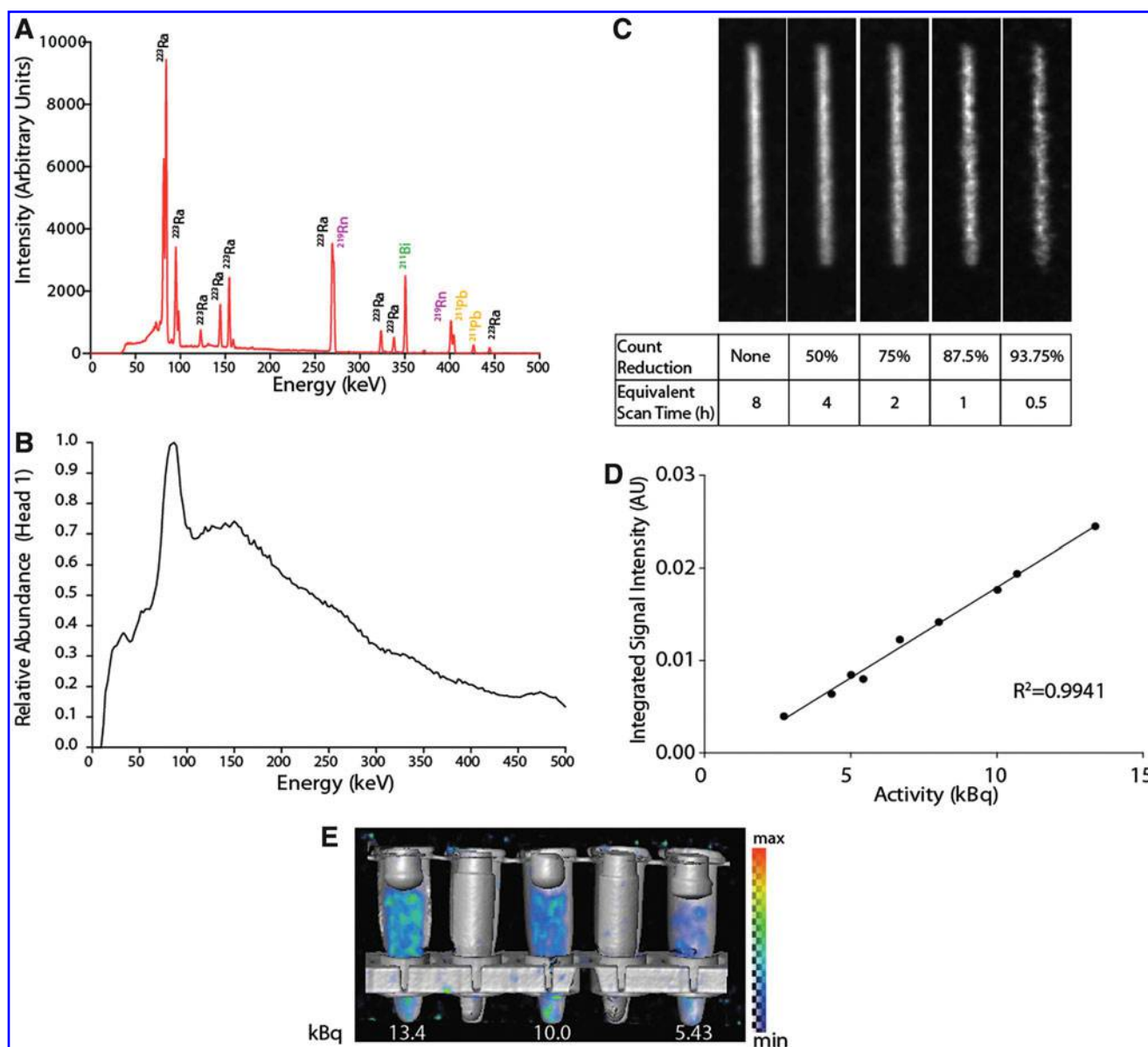


FIG. 1. (A) γ -spectrum of radium-223 and daughters acquired using a HPGe detector. The most abundant emissions are the ^{223}Ra emissions in the range of 75–100 keV. (B) The energy resolution of the sodium iodide γ -camera is significantly poorer than the HPGe, but still clearly resolves the ^{223}Ra photo peaks nearing 100 keV. (C) Images of three-dimensional reconstructed line phantoms of ^{223}Ra (using an energy window of 75–100 keV) with decreasing count reduction parameters. (D, E) Linear response with ^{223}Ra activity and user-defined volumes of interest, and representative fusion SPECT/CT image, respectively. CT, computed tomography; HPGe, high-purity germanium; SPECT, single photon emission computed tomography.

when passing through a biological medium. To determine the effect of scattering material on the system line response function, we imaged a line source in air and embedded in 99% water hydrogel approximating the diameter of a 25 g mouse (Fig. 2A–C). The count profiles across the 0.5 mm inner diameter capillary tubes varied only slightly, with full-width half-max (FWHM) values of 1.21 and 1.31 mm in air and 1.28 and 1.41 mm in gel in the vertical and horizontal directions, respectively. This compares favorably with the vendor provided reconstructed FWHM resolution of <1.1 mm for this collimator using the 140.5 keV emitting $^{99\text{m}}\text{Tc}$.

In vivo theranostics of radium-223

To investigate the *in vivo* distribution of ^{223}Ra , we first imaged mice after blood pool clearance and uptake at sites of active bone remodeling (Fig. 3). Animals ($n=4$) were administered between 20.3 and 26 kBq (0.55–0.7 μCi) by retro-orbital injection and imaged 24 h later, when the activity had cleared from the soft tissues.¹⁴ As can be seen in a representative subject, SPECT, CT, and fusion images reveal intense localization to the ends of the sites with the highest rates of bone formation and remodeling. This was demonstrated most clearly in the trabecular bone compartment of

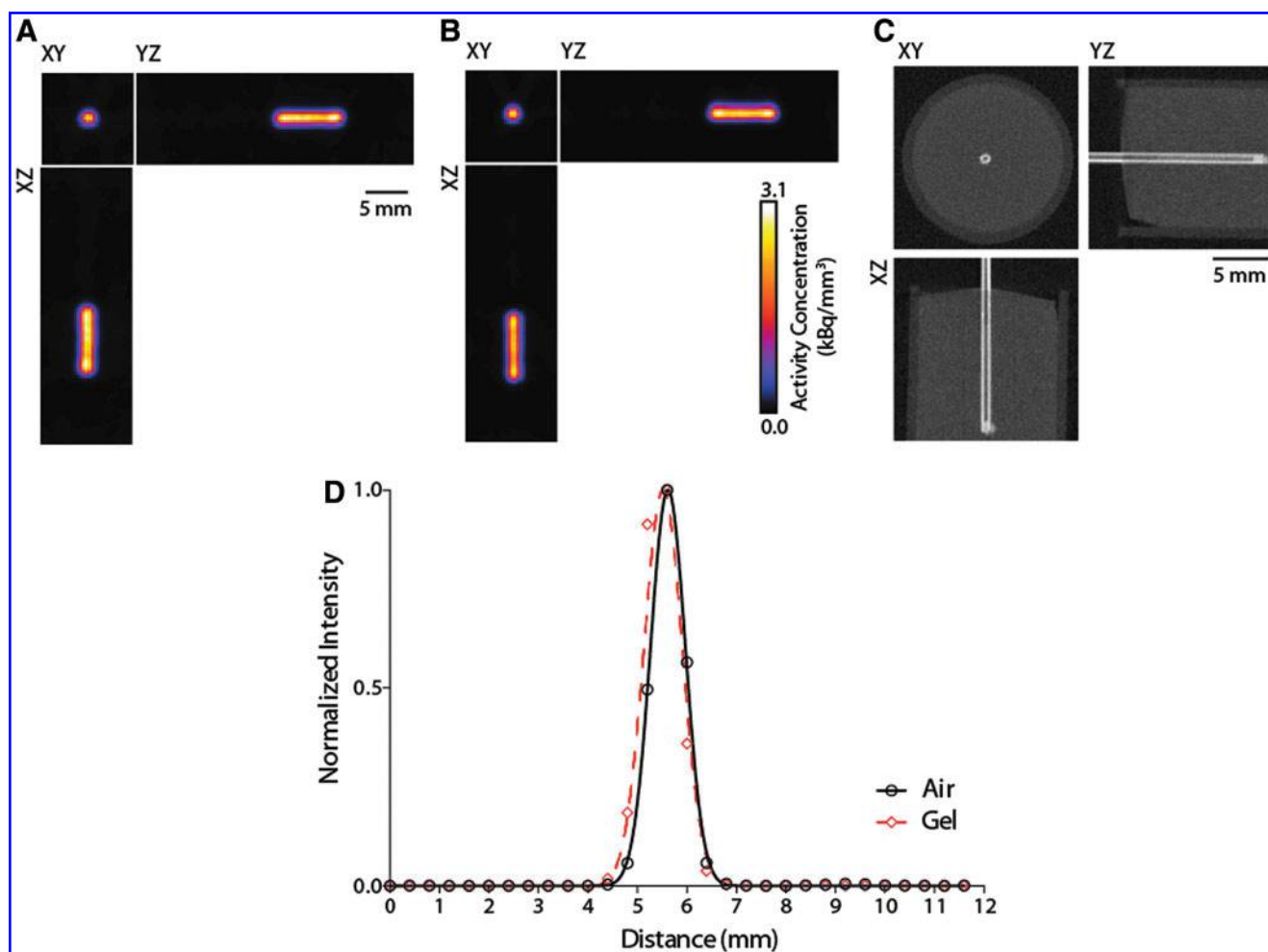


FIG. 2. Axial, coronal and sagittal slices through the reconstructed rod phantom in (A) air and (B) embedded in a 99% water hydrogel to simulate scattering from tissue. Volumes were both reconstructed with 8 subsets and 10 iterations using an iterative pixel-based ordered subset expectation maximization algorithm. (C) CT of the 1 mm external diameter rod source embedded in the hydrogel. Scale bar for all images is 5 mm. (D) Intensity profile in air (black) and gel (red dashed) of the horizontal profile across the capillary tube.

the distal tibia and proximal femur (Fig. 3A–C). In addition, signal from ^{223}Ra is apparent in the mandible and premaxilla and the proximal humerus and distal forelimb. Reconstructed SPECT volumes overlaid with CT reveal the capacity for whole-body tomographic imaging of uptake at sites of interest throughout the skeleton (Fig. 3D, E). Furthermore, as expected, the imaged distribution closely matches that seen using $^{99\text{m}}\text{Tc}$ medronic acid, the commonly used radiolabeled bisphosphonate bone scan tracer (Supplementary Fig. S1).

Ex vivo correlation of radionuclide distribution and radiobiological effect

To verify the noninvasive SPECT images, we performed unfixed, undecalcified whole mount whole-body cryo-sectioning and autoradiography. A color macrograph of the animal was acquired en bloc before sectioning (14 μm thickness) and transferred to a storage phosphor sheet for autoradiography (Fig. 3F–H). Consistent with reconstructed SPECT volumes, the overlay image clearly recapitulates the accumulated ^{223}Ra throughout the skeleton, notably at the manubrium of the ribcage, lower mandible, and hind limbs.

Magnified images of the midsection are shown at the right knee and left femoral midshaft (Fig. 3I, J).

Closer analysis of the leg was performed to assess correlation of imaging results and radiotherapeutic effect. SPECT/CT imaging of the lower hind limb shows intense uptake at proximal tibia and distal femur at 24 h (Fig. 4A–C). The leg was resected a day after the imaging study and en bloc imaging, autoradiography, and immunohistochemistry were performed (Supplementary Fig. S2). Labeling was most evident in the rapidly mineralizing bone of the metaphysis. We subsequently evaluated therapeutic effect by annotating DNA damage with immunofluorescence microscopy in treated and control animals (Fig. 4D, E). Sites of phosphorylated γH2AX were found throughout the trabecular bone compartment of the proximal femur in the treated animals in comparison with the low background staining in untreated control samples.

Imaging of transient radiotherapy

Our attempts at kinetic imaging of the low injected activities of ^{223}Ra were not successful because of extremely

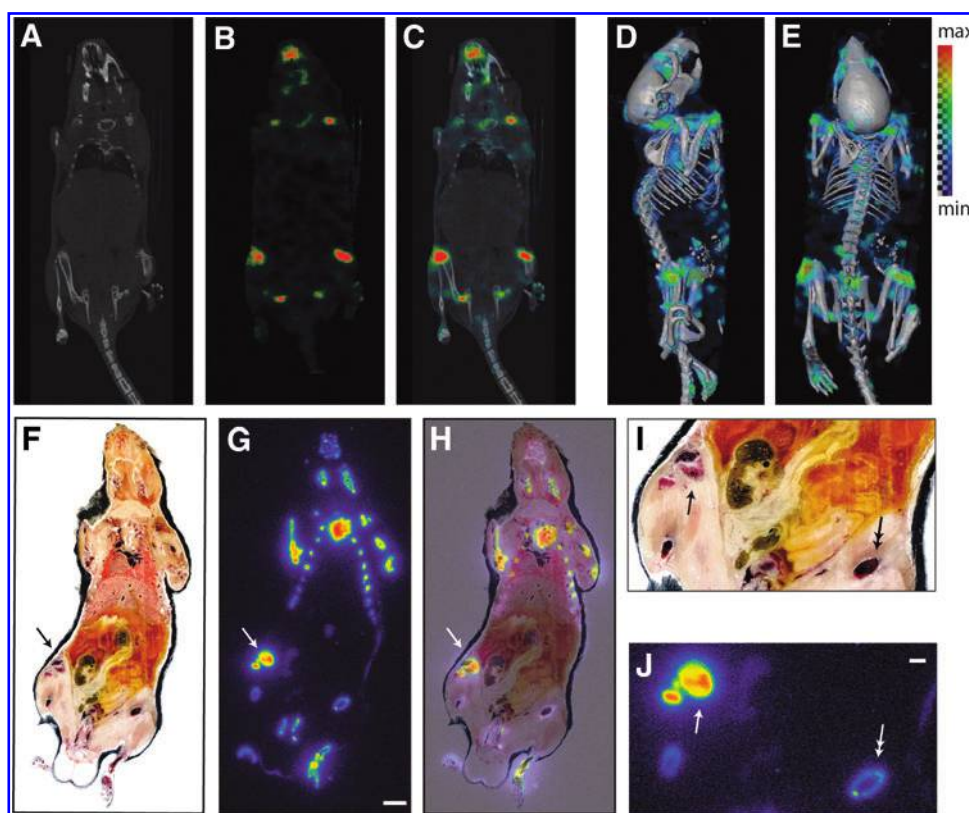


FIG. 3. Radium-223 SPECT/CT and whole-body autoradiography at 24 h postinjection. (A) CT, (B) SPECT, and (C) fused coronal slice of a mouse imaged 1 d after intravenous administration of 22 kBq $^{223}\text{RaCl}_2$ citrate. Four 22 min SPECT acquisitions were acquired and averaged, followed by a CT scan. (D, E) Lateral and dorsal views of three-dimensional volume rendered SPECT data overlaid onto surface rendered CT data. To generate this image, a weighted average of the intensities along projections through the SPECT volume was blended with the CT rendered image. Both slice and three-dimensional rendered volumes reveal intense uptake at the ends of the long bones and premaxilla. To confirm *in vivo* SPECT results, whole-body undecalcified cryosections ($14\mu\text{m}$) were obtained after imaging. (F) En bloc color macrograph, (G) autoradiography, and (H) overlay (scale bar, 5 mm). (I, J) Magnified images of the uptake at the midsection (scale bar, 2 mm). Arrow indicates the right knee; double-headed arrow, the ^{223}Ra uptake along the femoral shaft.

low detected counts. However, static imaging of subjects at defined intervals after injection can be used to approximate distribution at arbitrary time points. As an example, 2 min after administration of a 16 kBq ($0.43\mu\text{Ci}$) dose, the animal was killed, and imaged (Fig. 5A–E). At this early time point, the agent was detected in the heart. After SPECT/CT, the animal was rapidly cryosectioned and processed for autoradiography (Fig. 5F–H). Pooled activity in the heart and vena cava were identified, in addition to incomplete labeling of the skull.

Discussion

The increasing interest in the use of α -particle-emitting radionuclides for cancer cell therapy and ablation is an exciting development in the field of nuclear medicine. A key element in realizing the potential of this emerging strategy is to refine dosing parameters for maximized therapeutic effect with minimized toxicity. Tomographic imaging can play a significant role in achieving improved pharmacokinetic modeling and dose optimization of radionuclide tracers and therapeutic compounds but has largely not been possible for α -particle-emitting radionuclides.

Several scintigraphic imaging studies have been performed with α -particle-emitting therapies, including $^{223}\text{Ra}^{8-11}$ and antibody-labeled $^{213}\text{Bi}^{23}$. These have been important to reveal pharmacokinetic biodistribution and provide a first estimate of absorbed dose of these potent therapies in the clinical setting. The primary advantage of a SPECT is to remove out-of-plane information, rather than the planar images consisting of projections of the 3D activity distribution. SPECT provides improved contrast, resolution, and the capacity for true quantitation. Here, we evaluated the imaging characteristics and *in vivo* imaging capabilities of a dedicated small animal SPECT system possessing high sensitivity.¹⁶ This study demonstrates that the acquisition of noninvasive, quantitative, tomographic distribution of radium-223 can be achieved using dedicated preclinical equipment. Our investigations at early and late time points show that this approach is feasible and provides a means to evaluate radionuclide distribution with reasonable temporal resolution.

Phantom studies demonstrated that using an energy window of 75–100 keV sub-microcurie activities of ^{223}Ra could be imaged in three dimensions with near-millimeter spatial resolution over reasonable data acquisition times. The linear

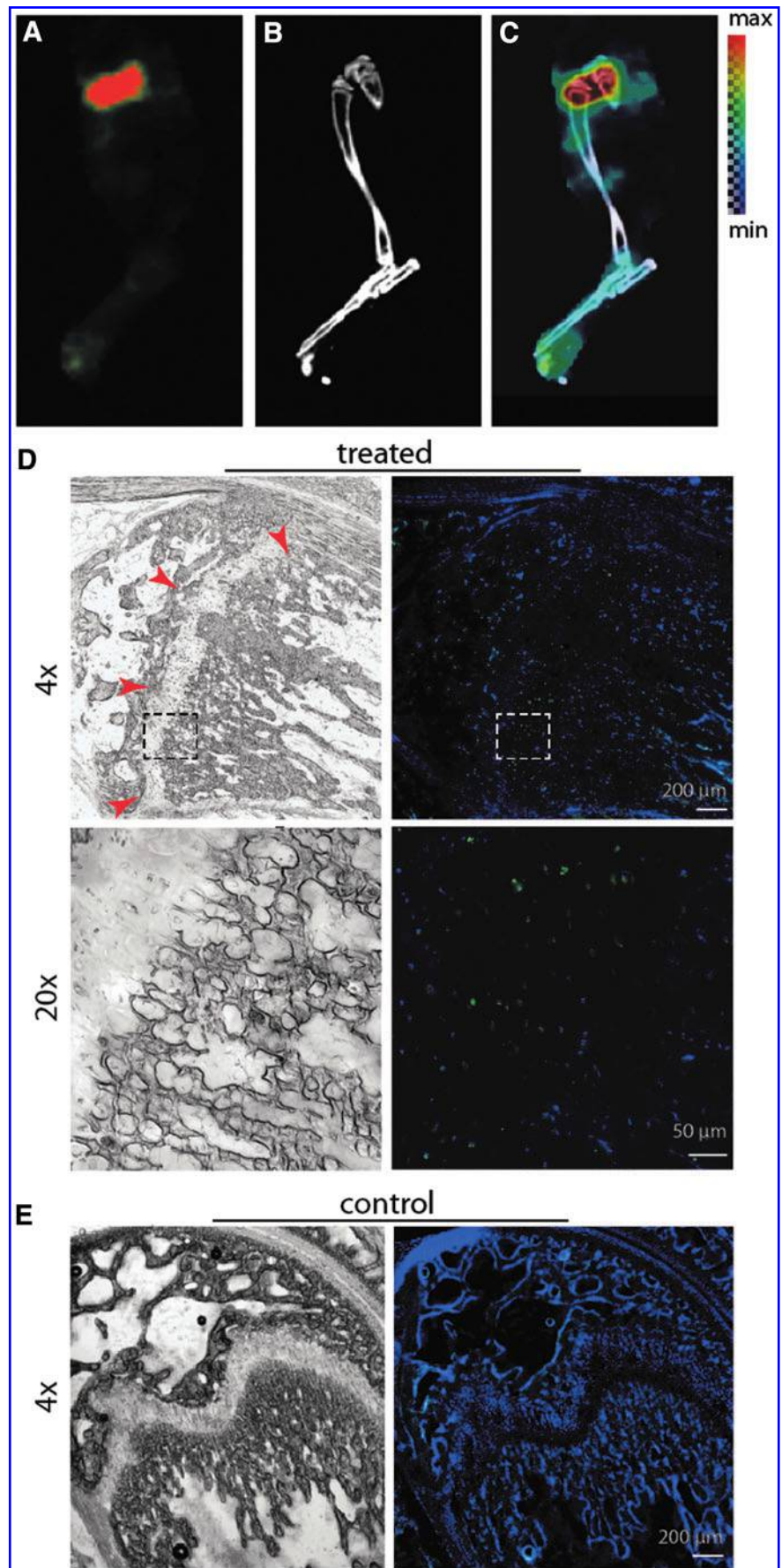


FIG. 4. (A) SPECT, (B) CT and (C) fusion of ^{223}Ra in the lower hind limb. Uptake is seen at the ends of the long bones where bone turnover and ossification are localized. *White light* (left) and phosphorylated γH2AX immunofluorescence staining (right) of the femoral head in (D) ^{223}Ra -treated and (E) control mice. Foci of phosphorylated γH2AX staining are identified throughout the bone forming front of the treated animals (red arrows).

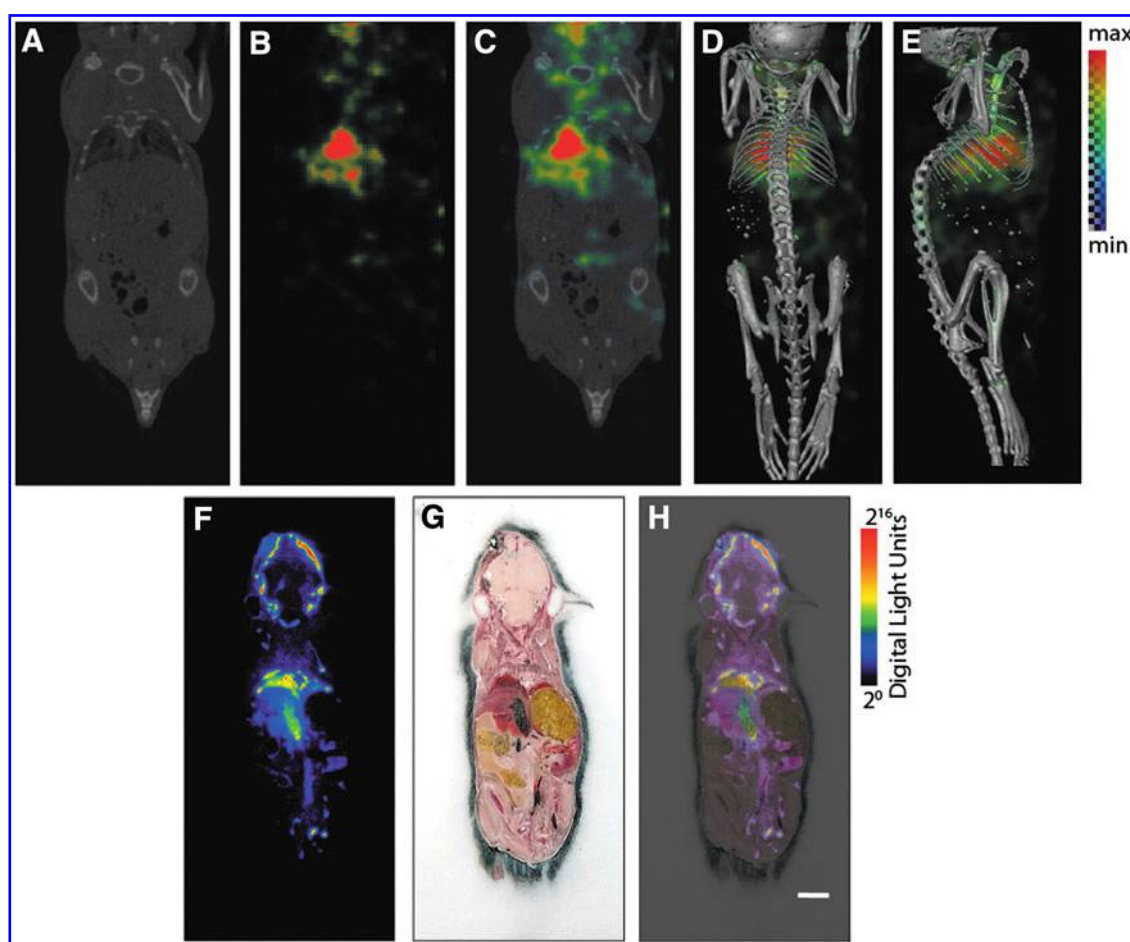


FIG. 5. Radium-223 SPECT/CT and whole-body autoradiography immediately after administration. *In vivo* (A) CT, (B) SPECT, and (C) fused coronal slice of a mouse killed 2 min postinjection of $^{223}\text{RaCl}_2$. (D) Tomographic SPECT/CT fusions at dorsal-ventral and (E) lateral projections. (F–H) Autoradiogram of cryosectioned whole animal, en bloc macrograph, and fusion.

response with activity in the investigated region can be used to determine activity concentrations non-invasively. As expected, ^{223}Ra labels the sites of active bone remodeling throughout the skeletal compartment. The noninvasive *in vivo* imaging performed well to highlight areas of intense uptake, such as at the mineralizing front of the metaphysis in the long bones, without the onerous requirements of fresh-frozen cryosectioning and autoradiography. The cytotoxic effects of the four α particles produced by ^{223}Ra and daughter radionuclides require further study to optimize activity amounts and scheduling in patients. Should administered activity levels depend on disease features rather than patient mass; should dosing frequency be increased or decreased; are there synergistic or toxic combinations that change pharmacokinetic properties? We have shown that imaging correlates with immunofluorescent localization of DNA damage, which directly measure effect, may inform upon these questions.

Limitations of this study include the low signal-to-noise and the limited field of view of the system. The former can be overcome with higher injected activity, amounts that may also enable more rapid dynamic imaging. Although such doses may indeed be tolerated with only mild toxicity,²⁴

they severely deviate from clinical practice. Furthermore, background readings made from the system indicate the suboptimal shielding of the γ -camera detectors of the SPECT in our animal facility (containing other photon-emitting radioactive animals within several meters distance). With improved facility management, one could expect improved signal-to-noise. Similarly, optimization of computational corrections for the spectral and subject properties (scatter and attenuation) and for reconstruction parameters may increase quantitative accuracy of the tomographs.

The second issue, relating to the small field of view, is a system-dependent parameter. The imageable volume consists of a large number of collimator-magnified projection images focused within the subject, and whole-body coverage is provided by bed motion through the detector. Redesigned collimators may enable the functional imaging of larger subjects, such as mature mice of interest for research study. ^{213}Bi sub-millimeter SPECT was recently reported using a similar small animal system and a dedicated high-energy collimator.¹⁵ Additional improvements in dedicated high-resolution detectors will improve both sensitivity and resolution.

Future work will focus on the definition of optimal energy windows to maximize the recovery coefficient and sensitivity-versus-resolution tradeoffs of the SPECT system and implementation of attenuation compensation. Concurrent developments in collimator design, reconstruction parameters, and detectors will enhance the scientific utility of these findings. The present investigations also have import beyond a specific radionuclide, and suggest that other investigational α -particle-emitting agents can be quantitatively imaged at low doses.

There are considerable differences between murine and clinical imaging parameters and considerations for the potential for quantitative imaging in men are significant. The administered activities per mass used in this work are greater than those approved for use in patients. However no deleterious effects were apparent at bodyweight normalized administered activities four-fold higher than the approved dose in a planar pharmacokinetic study,⁹ in which dynamic imaging of excretion through the gut was monitored. Increased scatter and attenuation of signal from patients may degrade image quality significantly and initial efforts are underway to simulate and image phantoms and patients.^{25–27} The use of noninvasive imaging as a means to predict and monitor therapeutic effect will enhance preclinical evaluation of altered dosing schedules and the role of combination treatments on ²²³Ra pharmacokinetics. We anticipate that these efforts will play a significant role toward improved patient treatment with ²²³Ra and other investigational α -particle emitters.

Authors' Contributions

Conceptualization, D.L.J.T.; Investigation, D.S.A., A.R., R.E.T., P.A.F., A.K.J., B.W.S., D.L.J.T.; Data analysis, A.R., B.W.S., D.U., R.C.R., D.L.J.T. Writing, All Authors; Supervision, B.T., D.L.J.T.

Disclosure Statement

There are no existing financial conflicts.

Funding Information

This work was supported in part by the Society of Nuclear Medicine and Molecular Imaging Junior Faculty Development Award (D.S.A.), Steve Wynn Prostate Cancer Foundation-Young Investigator Award (D.L.J.T.) and David H. Koch PCF-YIA (D.U.); Knut and Alice Wallenberg Foundation (D.U.); Bertha Kamprad Foundation (D.U.); Patrick C. Walsh Foundation (D.L.J.T.) and the National Institutes of Health Johns Hopkins University Cancer Center Support Grant, P50-CA058236-19A1 (PI: Nelson), and R01CA201035, R01CA229893 (D.L.J.T.).

Supplementary Material

Supplementary Figure S1
Supplementary Figure S2

References

1. Siegel RL, Miller KD, Jemal A. Cancer statistics, 2016. *CA Cancer J Clin* 2016;66:7.
2. Tait C, Moore D, Hodgson C, et al. Quantification of skeletal metastases in castrate-resistant prostate cancer predicts progression-free and overall survival. *BJU Int* 2014;114:E70.
3. Gravis G, Boher JM, Fizazi K, et al. Prognostic factors for survival in noncastrate metastatic prostate cancer: Validation of the glass model and development of a novel simplified prognostic model. *Eur Urol* 2015;68:196.
4. Parker C, Nilsson S, Heinrich D, et al. Alpha emitter radium-223 and survival in metastatic prostate cancer. *N Engl J Med* 2013;369:213.
5. Hoskin P, Sartor O, O'Sullivan JM, et al. Efficacy and safety of radium-223 dichloride in patients with castration-resistant prostate cancer and symptomatic bone metastases, with or without previous docetaxel use: A prespecified subgroup analysis from the randomised, double-blind, phase 3 ALSYMPCA trial. *Lancet Oncol* 2014;15:1397.
6. Sartor O, Coleman R, Nilsson S, et al. Effect of radium-223 dichloride on symptomatic skeletal events in patients with castration-resistant prostate cancer and bone metastases: Results from a phase 3, double-blind, randomised trial. *Lancet Oncol* 2014;15:738.
7. Etcheberry EC, Araujo JC, Fox PS, et al. Prognostic factors in patients treated with ²²³Ra: The role of skeletal tumor burden on baseline ¹⁸F-fluoride PET/CT in predicting overall survival. *J Nucl Med* 2015;56:1177.
8. Pacilio M, Ventroni G, Cassano B, et al. A case report of image-based dosimetry of bone metastases with Alpharadin ((²²³Ra-dichloride) therapy: Inter-fraction variability of absorbed dose and follow-up. *Ann Nucl Med* 2016;30:163.
9. Carrasquillo JA, O'Donoghue JA, Pandit-Taskar N, et al. Phase I pharmacokinetic and biodistribution study with escalating doses of (2)(2)(3)Ra-dichloride in men with castration-resistant metastatic prostate cancer. *Eur J Nucl Med Mol Imaging* 2013;40:1384.
10. Hindorf C, Chittenden S, Aksnes AK, et al. Quantitative imaging of ²²³Ra-chloride (Alpharadin) for targeted alpha-emitting radionuclide therapy of bone metastases. *Nucl Med Commun* 2012;33:726.
11. Chittenden SJ, Hindorf C, Parker CC, et al. A phase 1, open-label study of the biodistribution, pharmacokinetics, and dosimetry of ²²³Ra-dichloride in patients with hormone-refractory prostate cancer and skeletal metastases. *J Nucl Med* 2015;56:1304.
12. Pacilio M, Ventroni G, De Vincentis G, et al. Dosimetry of bone metastases in targeted radionuclide therapy with alpha-emitting (²²³Ra-dichloride). *Eur J Nucl Med Mol Imaging* 2016;43:21.
13. Jadvar H, Challa S, Quinn DI, et al. One-year postapproval clinical experience with Radium-223 dichloride in patients with metastatic castrate-resistant prostate cancer. *Cancer Biother Radiopharm* 2015;30:195.
14. Abou DS, Ulmert D, Doucet M, et al. Whole-body and microenvironmental localization of Radium-223 in naive and mouse models of prostate cancer metastasis. *J Natl Cancer Inst* 2016;108:djv380.
15. de Swart J, Chan HS, Goorden MC, et al. Utilizing high-energy gamma-photons for high-resolution ²¹³Bi SPECT in mice. *J Nucl Med* 2016;57:486.
16. Ivashchenko O, van der Have F, Goorden MC, et al. Ultra-high-sensitivity submillimeter mouse SPECT. *J Nucl Med* 2015;56:470.
17. van der Have F, Vastenhouw B, Rentmeester M, et al. System calibration and statistical image reconstruction for ultra-high resolution stationary pinhole SPECT. *IEEE Trans Med Imaging* 2008;27:960.

18. Abou DS, Pickett J, Mattson JE, et al. A Radium-223 microgenerator from cyclotron-produced trace Actinium-227. *Appl Radiat Isot* 2017;119:36.
19. Browne E. Nuclear data sheets for A=215,219,223,227, 231. *Nuclear Data Sheets* 2001;93:763.
20. Branderhorst W, Vastenhouw B, Beekman FJ. Pixel-based subsets for rapid multi-pinhole SPECT reconstruction. *Phys Med Biol* 2010;55:2023.
21. Ogawa K, Harata Y, Ichihara T, et al. A practical method for position-dependent Compton-scatter correction in single photon emission CT. *IEEE Trans Med Imaging* 1991;10:408.
22. United States Nuclear Regulatory Agency Licensing Decision of Radium-223 Dichloride. Washington, DC: Government Printing Office; 2013. Online document at <https://www.nrc.gov/reading-rm/doc-collections/nuregs/brochures/br0117/13-01.pdf>.
23. Sgouros G, Ballangrud AM, Jurcic JG, et al. Pharmacokinetics and dosimetry of an alpha-particle emitter labeled antibody: ^{213}Bi -HuM195 (anti-CD33) in patients with leukemia. *J Nucl Med* 1999;40:1935.
24. Larsen RH, Saxtorph H, Skydsgaard M, et al. Radiotoxicity of the alpha-emitting bone-seeker ^{223}Ra injected intravenously into mice: Histology, clinical chemistry and hematology. *In Vivo* 2006;20:325.
25. Benabdallah N, Bernardini M, Bianciardi M, et al. (^{223}Ra)-dichloride therapy of bone metastasis: Optimization of SPECT images for quantification. *EJNMMI Res* 2019;9:20.
26. Owaki Y, Nakahara T, Kosaka T, et al. Ra-^{223} SPECT for semi-quantitative analysis in comparison with $\text{Tc-}^{99\text{m}}$ HMDP SPECT: Phantom study and initial clinical experience. *EJNMMI Res* 2017;7:81.
27. Takahashi A, Baba S, Sasaki M. Assessment of collimators in radium-223 imaging with channelized Hotelling observer: A simulation study. *Ann Nucl Med* 2018;32:649.

This article has been cited by:

1. A. Paden King, Frank I. Lin, Freddy E. Escorcia. 2021. Why bother with alpha particles?. *European Journal of Nuclear Medicine and Molecular Imaging* **376**. . [[Crossref](#)]
2. Natalia Herrero Álvarez, David Bauer, Javier Hernández-Gil, Jason S. Lewis. 2021. Recent Advances in Radiometals for Combined Imaging and Therapy in Cancer. *ChemMedChem* **22**. . [[Crossref](#)]
3. Diane Abou, Nadia Benabdallah, Wen Jiang, Lu Peng, Hanwen Zhang, Alexandria Villmer, Mark S. Longtine, Daniel L. J. Thorek. 2020. Prostate Cancer Theranostics - An Overview. *Frontiers in Oncology* **10**. . [[Crossref](#)]